Remote Sensing of Environment 250 (2020) 112033

Contents lists available at ScienceDirect

Remote Sensing of Environment

journal homepage: www.elsevier.com/locate/rse

Automated detection of rock glaciers using deep learning and object-based image analysis

Benjamin Aubrey Robson[a,*], Tobias Bolch[b], Shelley MacDonell[c], Daniel Hölbling[d], Philipp Rastner[e], Nicole Schaffer[c]

[a] Department of Geography, University of Bergen, Norway
[b] School of Geography and Sustainable Development, University of St. Andrews, UK
[c] Centro de Estudios Avanzados en Zonas Áridas (CEAZA), La Serena, Chile
[d] Department of Geoinformatics – Z_GIS, University of Salzburg, Austria
[e] Department of Geography, University of Zurich, Switzerland

A B S T R A C T

Rock glaciers are an important component of the cryosphere and are one of the most visible manifestations of permafrost. While the significance of rock glacier contribution to streamflow remains uncertain, the contribution is likely to be important for certain parts of the world. High-resolution remote sensing data has permitted the creation of rock glacier inventories for large regions. However, due to the spectral similarity between rock glaciers and the surrounding material, the creation of such inventories is typically conducted based on manual interpretation, which is both time consuming and subjective. Here, we present a novel method that combines deep learning (convolutional neural networks or CNNs) and object-based image analysis (OBIA) into one workflow based on freely available Sentinel-2 optical imagery (10 m spatial resolution), Sentinel-1 interferometric coherence data, and a digital elevation model (DEM). CNNs identify recurring patterns and textures and produce a prediction raster, or heatmap where each pixel indicates the probability that it belongs to a certain class (i.e. rock glacier) or not. By using OBIA we can segment the datasets and classify objects based on their heatmap value as well as morphological and spatial characteristics. We analysed two distinct catchments, the La Laguna catchment in the Chilean semi-arid Andes and the Poiqu catchment in the central Himalaya. In total, our method mapped 108 of the 120 rock glaciers across both catchments with a mean overestimation of 28%. Individual rock glacier polygons howevercontained false positives that are texturally similar, such as debris-flows, avalanche deposits, or fluvial material causing the user's accuracy to be moderate (63.9–68.9%) even if the producer's accuracy was higher (75.0–75.4%). We repeated our method on very-high-resolution Pléiades satellite imagery and a corresponding DEM (at 2 m resolution) for a subset of the Poiqu catchment to ascertain what difference image resolution makes. We found that working at a higher spatial resolution has little influence on the producer's accuracy (an increase of 1.0%), however the rock glaciers delineated were mapped with a greater user's accuracy (increase by 9.1% to 72.0%). By running all the processing within an object-based environment it was possible to both generate the deep learning heatmap and perform post-processing through image segmentation and object reshaping. Given the difficulties in differentiating rock glaciers using image spectra, deep learning combined with OBIA offers a promising method for automating the process of mapping rock glaciers over regional scales and lead to a reduction in the workload required in creating inventories.

1. Introduction

Globally, the cryosphere is in a state of rapid change, for example mountain glaciers have lost 335 ± 144 Gt of mass per year between 2006 and 2016 (Zemp et al., 2019). As a consequence, many regions of the world are expected to undergo changes in seasonal and long-term water availability (Kehrwald et al., 2008; Immerzeel et al., 2010; Piao et al., 2010; Huggel et al., 2020), with the strongest effects being felt in arid and semi-arid environments (Huss and Hock, 2018; Pritchard, 2019).

Rock glaciers are typically tongue- or lobate-shaped landforms, consisting of poorly sorted, angular debris and ice-rich sediments, are commonly found in semi-arid and arid mountains. Rock glaciers can contain significant amounts of ice and are a visible manifestation of permafrost (Barsch, 1996; Haeberli et al., 2006; Rangecroft et al., 2014; Jones et al., 2018a).

Rock glaciers are generally categorised as active rock glaciers that contain sufficient ground ice to permit measurable ice deformation and therefore surface movements, inactive rock glaciers or transitional rock glaciers that contain ice, but not enough to actively deform, and relict rock glaciers that contain minimal to no ice (Barsch, 1996; Cremonese et al., 2011; Colucci et al., 2019). Rock glaciers are more resilient to climate change than other components of the cryosphere as both the rocky material and the active layer insulate the ice contained within the landform. As such they may become an important future water source, especially for arid and semi-arid regions, where in some cases the

* Corresponding author.
E-mail address: benjamin.robson@uib.no (B.A. Robson).

https://doi.org/10.1016/j.rse.2020.112033
Received 19 February 2020; Received in revised form 21 July 2020; Accepted 4 August 2020

demand for water has been increasing while future climate scenarios predict a decrease in precipitation (Bolch and Marchenko, 2009; Azocar and Brenning, 2010; Rangecroft et al., 2015; Schaffer et al., 2019). Although studies are scarce, some estimates put current rock glacier contribution to annual streamflow as high as 13–30% for some catchments (Geiger et al., 2014; Schaffer et al., 2019). It is therefore important to create and maintain up-to-date and accurate inventories of rock glaciers.

Mountain glaciers can typically be semi-automatically delineated with high-resolution satellite imagery, such as Landsat, ASTER, or Sentinel-2 (Paul et al., 2013; Pope and Rees, 2014) using a combination of band ratios between the visible and shortwave infrared sections of the electromagnetic spectrum for clean glacier ice, and a mixture of topographic and Synthetic Aperture Radar (SAR) coherence datasets for debris-covered ice (Bolch et al., 2007; Racoviteanu and Williams, 2012; Paul et al., 2015; Robson et al., 2015). These methods are however not applicable to the identification of rock glaciers, which are both spectrally inseparable from the surrounding paraglacial terrain and are deforming at rates sufficiently low to maintain SAR coherence. Historically, the majority of rock glacier inventories have been created based on manual interpretation of aerial or very high-resolution satellite imagery. The earliest rock glacier inventories were produced solely using manual interpretation of aerial photography (Wahrhaftig and Cox, 1959; Outcalt et al., 1965; Gorbunov and Titkov, 1989). Manual interpretation of high-resolution satellite or aerial imagery relies on identifying surface features indicative of rock glaciers, such as furrows, ridges and steep frontal slopes, and separating them from the surrounding terrain (Jones et al., 2018b). High-resolution aerial photography in conjunction with high-resolution Digital Elevation Models (DEMs) has been used to create inventories of rock glaciers in several mountain ranges (Esper Angillieri, 2009; Scotti et al., 2013; Onaca et al., 2017).

The prohibitively high cost of sub-metre-scale satellite imagery and elevation products however means in regions without accessible national aerial photography datasets, Google Earth imagery is often the best alternative in case of limited budget, for example Rangecroft et al. (2014), Jones et al. (2018b), and Pandey (2019). The use of Google Earth imagery however impedes automation of workflows, and analysis is restricted to the manual creation of polygons within the software.

Many recent rock glacier inventories have been produced with the aid of auxiliary data, for example topographic datasets can be used to help distinguish rock glaciers by their morphology (Falaschi et al., 2014; Rangecroft et al., 2014; Bolch et al., 2019), while Differential Interferometric Synthetic-Aperture Radar (DInSAR) can be used to identify areas that are actively deforming (Liu et al., 2013; Barboux et al., 2014; Bodin et al., 2016; Necsoiu et al., 2016; Villarroel et al., 2018). DInSAR however cannot be directly used for automatically detecting rock glaciers due to its sensitivity to atmospheric disturbances and ability to only observe deformations in the satellite line of sight (LOS). Additionally foreshortening, layover, and shadowing can cause problems in mountainous terrain. Additionally, DInSAR is only able to distinguish actively deforming land surfaces which could include other kinds of surface deformations such as solifluction.

The creation of rock glacier inventories is often subjective, with results varying due to the datasets used, the image interpreter, and landform definitions chosen (Bolch and Gorbunov, 2014; Brardinoni et al., 2019). As such, an automated methodology is needed. Some studies have made advances in automated identification of rock glaciers. The methods developed thus far typically rely on surface textures or rock glacier morphological characteristics (Janke, 2001; Brenning, 2009; Brenning et al., 2012). To date, these methods have only been applied to regions with a relatively small number of rock glaciers and have not been widely applied to larger regions.

Finally, recent studies have used remote sensing data combined with existing rock glacier inventories to distinguish active rock glaciers from inactive and relict rock glaciers. Bertone et al. (2019) used multi-temporal Sentinel-1 derived backscatter and coherence rasters to differentiate between moving and non-moving rock glaciers. Similarly, Kofler et al. (2019) used Sentinel-2 imagery, a LiDAR DTM within three classifiers (logistic regression (generalized linear model – GLM), support vector machine (SVM) and random forest (RF)) and assigned rock glaciers in the South Tyrolean Alps in Italy to be either intact or relict.

Convolution Neural Networks (CNNs), also known as deep learning, in conjunction with Object-Based Image Analysis (OBIA) presents a possibility for automated identification of rock glaciers. CNNs are a branch of machine learning that are increasingly being applied to remotely sensed imagery. CNNs rely on large sample datasets to train the algorithm to recognise recurring patterns within datasets and are typically utilised in applications where spectral characteristics are not sufficient, such as landslides and avalanches (Ding et al., 2016; Yu et al., 2017; Bianchi et al., 2019; Ghorbanzadeh et al., 2019), permafrost thaw slumps (Huang et al., 2020), urban mapping (Längkvist et al., 2016; Mahdianpari et al., 2018; Zhang et al., 2018), and ship identification in various sea and ice conditions (Bentes et al., 2016; Gallego et al., 2018).

OBIA is an image analysis method that relies on near-homogeneous objects created through image segmentation as the basis for classification, as opposed to individual pixels. Analysis at the object-level rather than the pixel-level allows classifications to utilise contextual, hierarchical, and spatial characteristic of image objects in addition to solely using spectral information. In recent years OBIA has proven to be a useful method for automating the delineation of natural phenomena including clean-ice and debris-covered glaciers (Rastner et al., 2013; Robson et al., 2015). Using CNNs together with OBIA is likely to provide a novel and powerful technique to automatically identify rock glaciers in mountainous landscapes.

The main objective of this study is to develop a novel method based on deep learning and OBIA to extract the location and extent of rock glaciers in two catchments, namely the La Laguna catchment in Northern Chile, and the Poiqu catchment in Central Himalaya. We ascertain the accuracy and transferability of our Convolutional Neural Network Object-Based Image Analysis method by comparing our results with reference outlines of rock glaciers based on manual interpretation of orthorectified Pléiades imagery (henceforth referred to as RG_Man). We assess both Sentinel 2 imagery (spatial resolution 10 m, henceforth referred to as CNN_OBIA) and very-high resolution Pléiades imagery (resolution 0.5 m, resampled to 2 m, henceforth referred to as CNN_OBIA_Ple).

2. Background – deep learning

Deep learning is a rapidly emerging area within the fields of remote sensing and geoinformatics (Zhang et al., 2016; Li et al., 2018; Ma et al., 2019). Deep learning, as well as other machine learning or artificial intelligence methods, attempt to interpret imagery in the same way as a human operator would, relying not only on pixel values but reoccurring patterns and textures (Ma et al., 2019). As such, deep learning can be used to extract information from complex situations where normal classification methods are not sufficient (Li et al., 2018).

In this study we restrict our analysis to CNNs which are the most widely used deep learning model and are well suited to multispectral satellite imagery (Ma et al., 2019). CNNs are made up of three components: convolution layers, pooling layers, and fully connected layers. The input data, for example a multispectral image, is first convolved with a moving window of a fixed size (for example a 5×5 or 3×3 pixel kernel). This then creates the first convolution layer. Each kernel is repeated several times, each one looking for a different distinct texture or pattern. These are referred to as feature maps. A convolution layer is often expressed in terms of its pixel size in X and Y dimensions, and its number of feature maps in the Z dimension, for example, a convolution of $5 \times 5 \times 40$ refers to an image being convolved by a 5×5 kernel producing 40 feature maps.

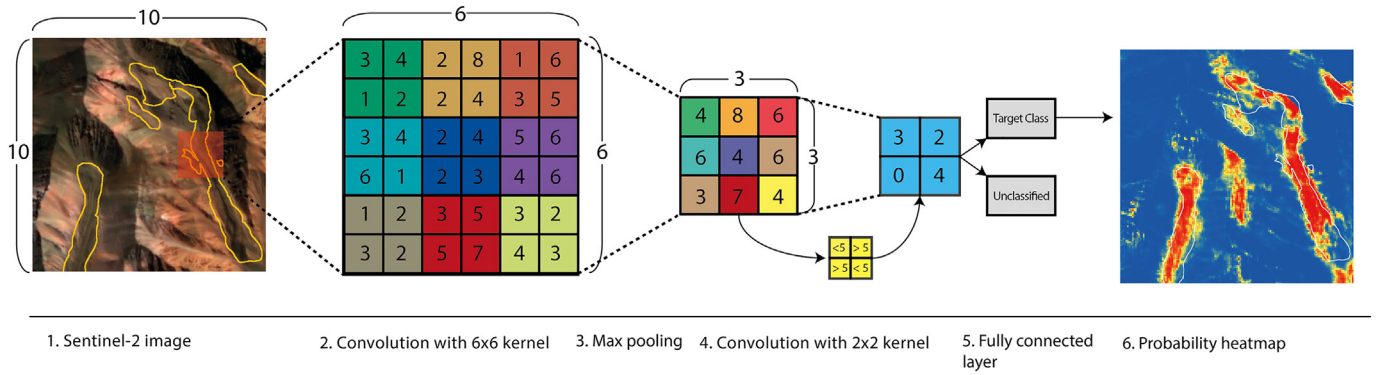

Fig. 1. A simplified example of a Convolutional Neural Network workflow. A convolution based on a 6 × 6 moving window is applied to an input image, resulting in the first convolutional layer. Max pooling, and an additional convolution are then applied. The heatmap shows the probability that a pixel belongs to a given class. Note that the process has been simplified and most CNNs would involve additional convolution and pooling layers, feature maps, and additional input bands.

CNNs are typically composed of multiple convolution layers. These convolution layers are often interspaced by pooling layers (Fig. 1). A pooling layer acts to aggregate pixels in a layer, thereby producing a new layer of reduced dimensions. The most common type of pooling, and the type used in this analysis, is max pooling. Max pooling simply uses a 2 × 2 kernel and takes the highest value and outputs it to the new layer. Lastly, a fully-connected layer brings all the previous layers together, and determines which feature maps are most useful at identifying the landform or class that the CNN is aiming to classify (for example a rock glacier). The output from a fully-connected layer is a prediction raster, also known as a heatmap, where pixels range between 0 and 1, with higher values indicating a given pixel has a greater certainty of belonging to the desired class. A simplistic schematic explanation of a CNN is shown in Fig. 1.

2.1. Object-based image analysis (OBIA)

OBIA is an established method within remote sensing (Blaschke et al., 2014). OBIA works by segmenting imagery into near-homogeneous objects, which serve as the basis for subsequent classification. Image segmentation is perhaps the most critical step within OBIA and can strongly influence the final classification result (Drăguţ et al., 2014; Jozdani and Chen, 2020). If the objects created are too large then multiple features can be treated as single objects, while too small objects reduce the effectiveness of using shape and contextual constraints within the classification (Rastner et al., 2013; Robson et al., 2015). Image segmentation is a bottom-up process, where additional image-object levels can be created by segmenting existing image objects.

Conducting the analysis at the object-level rather than the pixel-level allows spatial, contextual, hierarchical and textural information to be used instead of solely relying on spectral reflectance values (Lang, 2008). Additionally, OBIA permits the integration of many data types (optical, radar, topographic, point cloud, vector) within the analysis. OBIA has been shown to be well-suited for the mapping of natural phenomena such as debris-covered glaciers (Rastner et al., 2013, Robson et al., 2015), landslides (Hölbling et al., 2012; Hölbling et al., 2016) and flood extents (Mallinis et al., 2013; Dao and Liou, 2015). By utilising the spatial and contextual properties of image objects, it is possible to automate an element of the classification post-processing using OBIA, for example removing irregularly shaped, or asymmetrical image objects (Rastner et al., 2013, Robson et al., 2015).

3. Study sites and data

3.1. Study area

We conducted our analysis in two distinct periglacial catchments (Fig. 2). The study areas were chosen due to the availability of VHR Pléiades satellite imagery, as well as each site including rock glaciers of a variety of sizes and activity.

3.1.1. La Laguna catchment, Chile

The La Laguna catchment (~30°11'53 S, 69°56'15 W) is situated at the headwaters of the Elqui River catchment, with glaciers and rock glaciers contributing between 4 and 13% of the annual streamflow (Favier et al., 2009; Pourrier et al., 2014). The study area is situated between ~4000 and 6000 m a.s.l. The catchment is ~140 km^2 in size and contains 105 rock glaciers (~ 14.8 km^2) according to the Chilean National Water Directorate (DGA) inventory. Tapado Glacier (1.26 km^2) is the largest glacier in the catchment and contains a clean ice section, a debris-covered glacier section, and a rock glacier tongue. Precipitation falls mainly as snow and is concentrated within the austral winter. The area is semi-arid and cold, and at an elevation of approximately 3100 m a.s.l. has a mean precipitation rate of 167 mm per year measured between 1970 and 2009, and a mean annual air temperature (MAAT) of 8 °C between 1974 and 2011. The MAAT has been reported to be rising by 0.17 °C per decade between 1974 and 2011 (Monnier et al., 2014).

3.1.2. Poiqu catchment, Central Himalaya

The Poiqu catchment (~28° N, 85° E) is a transboundary watershed that drains through the Himalayas to Nepal and ultimately into the river Ganges. The catchment has a drainage area in excess of 2000 km^2 and ranges in elevation from ~1100 to > 8000 m a.s.l. (Mt. Shishapangma, 8027 m). It contains an assortment of clean-ice, debris-covered glaciers, and rock glaciers. The mean annual precipitation (measured at Nyalam, 3750 m a.s.l.) is ~650 mm and is influenced by the Indian monsoon, with most precipitation falling in the autumn (September to November). Mean annual temperatures at Nyalam range from 10.7 °C to −3.4 °C with temperatures typically below freezing between November and March (Xiang et al., 2014). We restricted our study to approximately 1500 km^2 of the Poiqu catchment that according to the inventory created P. Rastner (Bolch et al., 2020) contains ~140 rock glaciers (~ 21 km^2 in total) with sizes varying from < 0.01 to > 1 km^2. A smaller subset (~ 63 km^2) centred around the Mulaco massif in the centre of Poiqu catchment, an area that contains a total rock glacier area of 3.5 km^2, was chosen for repeating the analysis using Pléiades imagery. The areas processed for both subsets are shown in Fig. 2.

3.2. Data

For both study areas, we used freely available Sentinel-2 imagery (Blue, Green, Red, NIR and SWIR bands) as well as SAR coherence data generated from interferometric Sentinel-1 imagery (Table 1). We included the coherence data as the lower coherence values over debris-

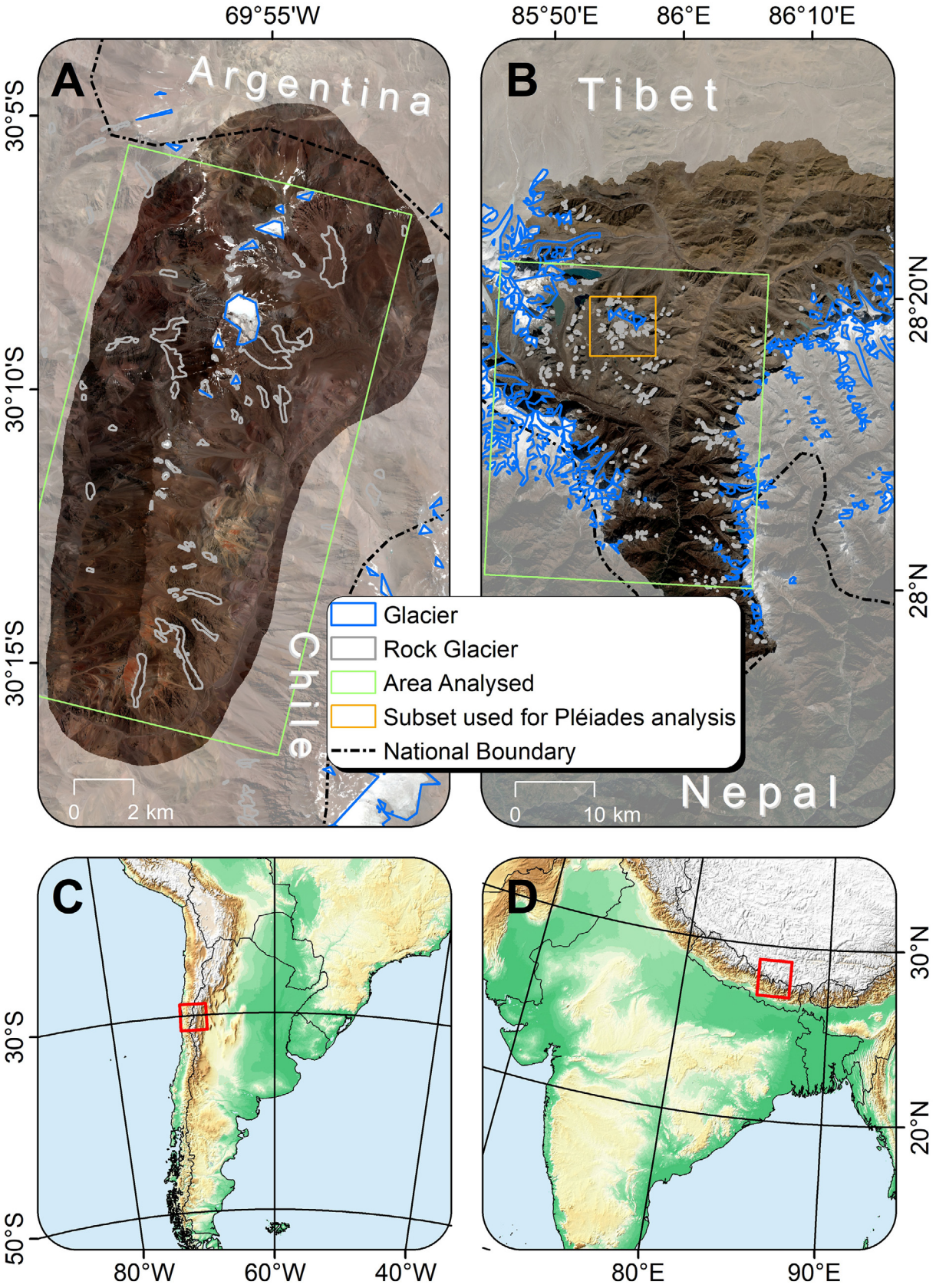

Fig. 2. Overview of the study sites, namely La Laguna catchment in the semi-arid Chilean Andes (A) and the Poiqu catchment on the Tibetan Plateau with the subset used for the Pléiades analysis highlighted (B). The approximate locations of the two study sites within South America and the Indian subcontinent are shown in (C) and (D). Glacier outlines shown are from the Randolph glacier inventory (Pfeffer et al., 2014), rock glacier outlines are from the Schaffer and Macdonell (2020) inventory for A and from Bolch et al. (2020) in B. In both A and B, Pléiades satellite imagery overlaying Sentinel-2 imagery is shown. The background data for C and D are elevation tinted hillshade models accessed through ArcGIS Online. Pléiades, 2018–9, different acquisition dates, © CNES (2018), and Airbus DS (2018), all rights reserved.

Table 1
Data used in this study. Pan refers to the panchromatic band, SWIR refers to the shortwave infrared band, MS refers to multispectral bands. Note that for sensors that contain bands of different resolution, both are given.

Date	Sensor	Scene ID	Spatial resolution (m)	Purpose
La Laguna catchment				
20.04.2019	Sentinel-1	S1B_IW_SLC__1SDV_20190420T232000_20190420T232027_015896_01DDD0_92A7	5 × 20	SAR coherence generation
08.04.2019	Sentinel-1	S1B_IW_SLC__1SDV_20190408T231959_20190408T232027_015721_01D808_F654	5 × 20	SAR coherence generation
31.01.2019	Pléiades	DS_PHR1A_201901231457145_FR1_PX_W070S31_0120_01956	0.5 (pan), 2 (MS)	DEM generation
04.04.2018	Sentinel-2	S2A_MSIL1C_20180404T143751_N0206_R096_T19JCG_20180404T180352	10 (20 SWIR)	Image classification
04.04.2018	Sentinel-2	S2A_MSIL1C_20180404T143751_N0206_R096_T19JDG_20180404T180352	10 (20 SWIR)	Image classification
Poiqu catchment				
04.11.2018	Pléiades	DS_PHR1A_201811040503518_FR1_PX_E085N28_1108_01768	0.5 (pan), 2 (MS)	DEM generation, image classification
03.11.2018	Pléiades	DS_PHR1B_201811030511344_FR1_PX_E085N28_0715_03053	0.5 (pan), 2 (MS)	DEM generation, image classification
22.10.2018	Pléiades	DS_PHR1B_201810220504174_FR1_PX_E086N28_0102_01804	0.5 (pan), 2 (MS)	DEM generation, image classification
15.10.2018	Pléiades	201810150507481_FR1_PX_E085N28_1103_02921	0.5 (pan), 2 (MS)	DEM generation, image classification
15.10.2018	Pléiades	DS_PHR1B_201810150507593_FR1_PX_E086N27_0123_00862	0.5 (pan), 2 (MS)	DEM generation, image classification
03.10.2018	Pléiades	DS_PHR1B_201810030500231_FR1_PX_E086N28_0309_02182	0.5 (pan), 2 (MS)	DEM generation, image classification
02.10.2018	Pléiades	DS_PHR1A_201810020508169_FR1_PX_E085N28_0911_05204	0.5 (pan), 2 (MS)	DEM generation, image classification
27.09.2018	Pléiades	DS_PHR1A_201809270456239_FR1_PX_E086N28_0510_01804	0.5 (pan), 2 (MS)	DEM generation, image classification
26.09.2018	Pléiades	DS_PHR1B_201809260504010_FR1_PX_E086N28_0105_05430	0.5 (pan), 2 (MS)	DEM generation, image classification
29.09.2017	Sentinel-1	S1A_IW_SLC__1SDV_20170925T122202_20170925T122230_018532_01F3B1_BE41	5 × 20	SAR coherence generation
10.07.2017	Sentinel-1	S1A_IW_SLC__1SDV_20171007T122203_20171007T122231_018707_01F8FC_032F	5 × 20	SAR coherence generation
12.09.2016	Sentinel-2	S2A_MSIL1C_20161209T045202_N0204_R076_T45RUM_20161209T045602	10 (20 SWIR)	Image classification
12.09.2016	Sentinel-2	S2A_MSIL1C_20161209T045202_N0204_R076_T45RUM_20161209T045602	10 (20 SWIR)	Image classification
12.09.2016	Sentinel-2	S2A_MSIL1C_20161209T045202_N0204_R076_T45RUL_20161209T045602	10 (20 SWIR)	Image classification
12.09.2016	Sentinel-2	S2A_MSIL1C_20161209T045202_N0204_R076_T45RVL_20161209T045602	10 (20 SWIR)	Image classification
25.09.2018	Pléiades	DS_PHR1A_201809250511185_FR1_PX_E085N28_1110_03316	0.5 (pan), 2 (MS)	DEM generation

covered glaciers helped separate them from rock glaciers, which can in some cases be spectrally similar.

All Sentinel data was downloaded through the Copernicus Open Access Hub. Topographic data is important in rock glacier mapping, and while a high-resolution, freely available DEM was available for the Poiqu catchment (namely the 8 m resolution High Mountain Asia DEM (Shean, 2017)) it was necessary to have consistent and comparable datasets for both study regions that would also be applicable at other sites for future implementation. For that reason, we used tri-stereo Pléiades satellite imagery from 2018 and 2019 to generate DEMs over both study areas (Table 1).

Reference rock glacier outlines were used for the generation of training data. For both study areas we used manually delineated outlines based on orthorectified Pléiades imagery and hillshade models based on the Pléiades DEMs. For the La Laguna catchment these were the outlines created by Schaffer and Macdonell (2020) and for the Poiqu catchment the outlines are those created by P. Rastner (Bolch et al., 2020).

It should be noted that in Chile, both glaciers and rock glaciers are typically incorporated into one inventory (Nicholson et al., 2009). As such, we excluded clean-ice glaciers from our analysis. We did, however, include two landforms (Tapado Glacier and an unnamed landform (CL104300033)) that have both an identified debris-covered glacier component as well as a rock glacier component (Monnier et al., 2014).

4. Methods

The methods used in this paper can be split into three sections (Fig. 3): (A) pre-processing of imagery and generation of training data, (B) image classification, and (C) post-processing and accuracy assessment. Full details about the thresholds and parameters used are given in Fig. 3. A combination of ArcGIS 10.7, eCognition 9.5, PCI Geomatica 2018, the European Space Agency's Sentinel Application Platform (SNAP) and Correlation Image Analysis Software (CIAS) (Kääb and Vollmer, 2000) were used.

4.1. Data pre-processing

The Pléiades tri-stereo stereo images were processed in PCI Geomatica 2018. DEMs were produced using the Rational Polynomial Coefficients (RPCs) provided with the imagery, as well as between 100 and 200 automatically generated tie points per tri-stereo pair. The DEMs were extracted at both 10 m and 2 m postings using a Semi-Global Matching algorithm, which has been shown to outperform normalised cross-correlation and thereby produce cleaner DEMs (Hirschmuller, 2007). For the Poiqu catchment, the resulting ten DEMs were mosaicked together. The multispectral imagery was panchromatically sharpened using a multi-resolution analysis (MRA) fusion that uses wavelet decomposition to preserve spectral fidelity (González-Audícana et al., 2005). The pan-sharpened images were then orthorectified and mosaicked together. As a prerequisite to running the CNN on the data, it was necessary to convert all the satellite imagery and DEMs into 32-bit floating rasters with pixel values normalised between 0 and 1.

SAR coherence rasters were generated for both study areas using SNAP. For each location, two Sentinel-1 single look complex (SLC) images in interferometric wide (IW) swath mode with a temporal baseline of 12 days were co-registered together using a DEM-assisted co-registration based on the Pléiades DEMs. The resulting image stacks were then deburst before the coherence was generated. The resulting rasters were then multilooked using ten pixels in range and two in azimuth, before being converted to ground range and exported as a GeoTiff.

The RG_Man outlines were used for training data. We extracted 30% of RG_Man for training data based on a random number generation. Given the small number of rock glaciers in the subset covered by the Pléiades imagery, 50% of the polygons were used as training. This resulted in 2.3 km^2 (n = 11) and 6.1 km^2 (n = 41) of rock glaciers for the La Laguna catchment and Poiqu catchment, respectively, and 0.7 km^2 (n = 8) for the Pléiades subset. The remaining polygons (n = 50 for La Laguna, n = 117 for Poiqu, n = 7 for Poiqu Pléiades subset) were used for accuracy assessment. In both study areas, adjacent rock glacier polygons were merged, and small polygons ($< 0.05\ km^2$) were removed. Approximately 300 random training points were generated within the rock glacier training outlines. Points were also generated for debris-covered glaciers, clean ice glaciers and stable (i.e. not related to fluvial, glacial or periglacial processes) terrain. All data were projected into UTM 19 S for La Laguna catchment, and UTM 45 N for the Poiqu catchment.

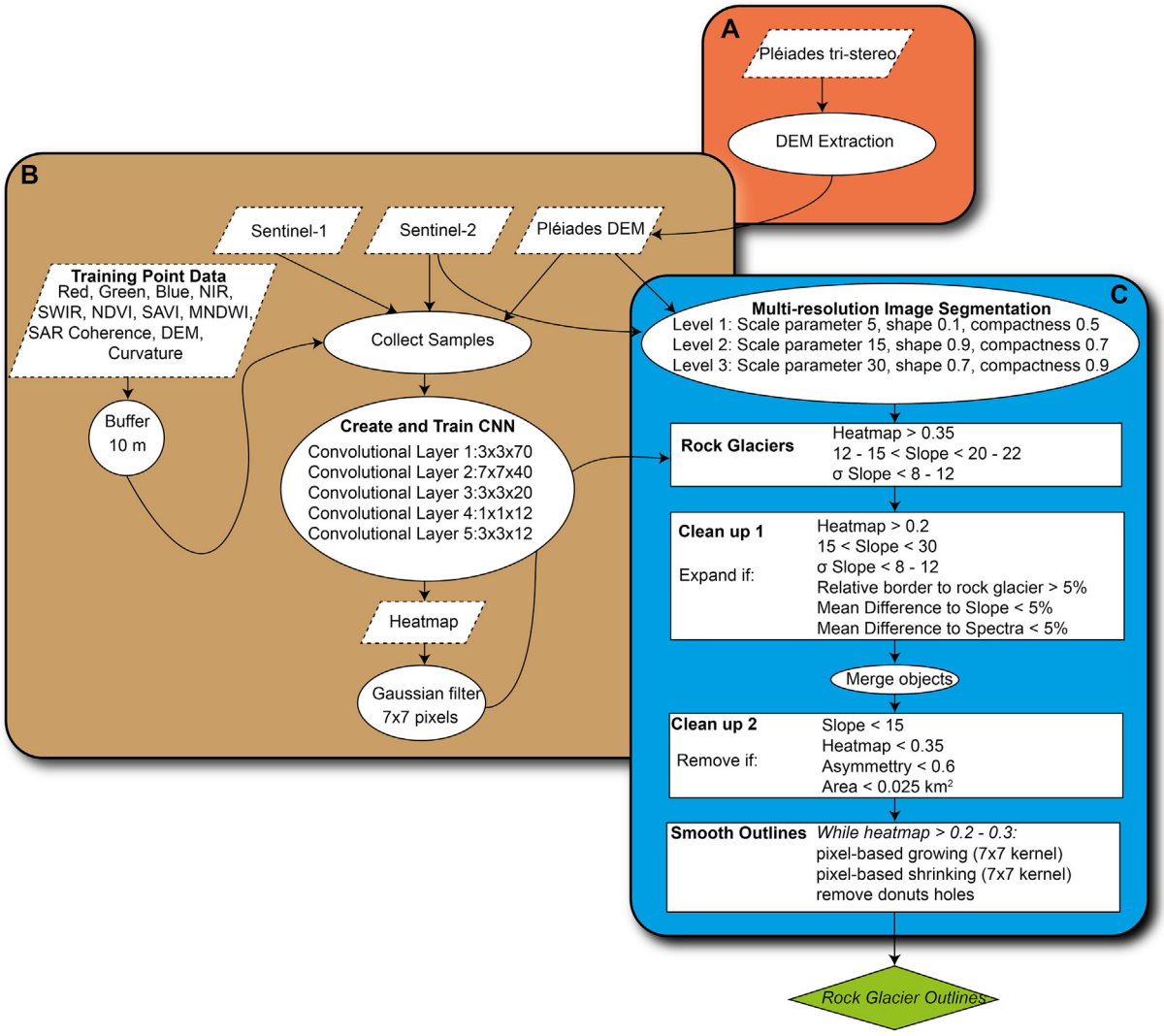

Fig. 3. Flowchart showing the methods used in this study. The methods can be split into three sections, the first (A) involved generating the Pléiades imagery to produce a DEM and the orthorectified mosaic, (B) the CNN workflow and (C) the OBIA refinement and reshaping. Acronyms used: NDVI (Normalised Difference Vegetation Index), MNDWI (Modified Normalised Difference Water Index) and SAVI (Soil Adjusted Vegetation Index). Criteria that have shown a range of thresholds reflect a fuzzy criterion.

4.2. Image classification

The entire image classification procedure (training of the CNN, applying to the entire imagery, OBIA reshaping) was conducted within eCognition 9.5 (Fig. 3). The CNN model used in this study, Google Tensorflow, is free and open source; however, by running the process through eCognition it was possible to have the CNN and OBIA re-shaping components in one seamless workflow.

4.2.1. Sentinel-2 analysis

We trained the CNN using the Sentinel 2 (Red, Green, Blue, NIR, SWIR), Sentinel-1 SAR coherence, as well as the DEM and curvature for the classes of *rock glacier, debris-covered glacier, clean ice, stable terrain,* and *shadows*. Additionally, we found it beneficial to also include the NDVI (Normalised Difference Vegetation Index), MNDWI (Modified Normalised Difference Water Index) (Xu, 2006) and SAVI (Soil Adjusted Vegetation Index) (Alba et al., 2011) within the analysis.

As a first step, the pixels with the lowest 5% reflectance in a mean of all the multispectral channels were classified as shadows and masked out. A 10-m buffer was constructed around the training point files for each and used to generate sample patches measuring 30 × 30 pixels using all the multispectral channels, the DEM and the curvature. Both the number of sample patches as well as the distribution of used can influence the output of a CNN. Some studies have chosen the number of sample patches per class based on the prevalence of each class (e.g. Guirado et al., 2017; Csillik et al., 2018; Zhang et al., 2020). In our case, we manually chose the number of sample patches used for training the model based on a combination of relative spectral distinction between classes (for example clean ice, debris-covered ice, and shadows requiring less samples than rock glaciers or stable ground) and the prevalence of a class (for example stable ground covering most of the image). Five thousand sample patches were collected for rock glaciers, 3000 for clean ice, debris-covered ice, and shadows, and 15,000 for stable ground.

It is still an ongoing debate within the machine learning community how to tune a CNN for optimal performance (Csillik et al., 2018; Schratz et al., 2019). In the absence of other studies that have applied CNNs to identify rock glaciers, we experimented with the simplest CNN architecture (a one-layer model) and adapted the kernel sizes, the number of convolutional layers and feature maps by a trial and error approach on the data covering the La Laguna catchment. In order to ascertain the transferability of our method we then applied the same ruleset on the Poiqu catchment without modifications. We found that having more convolutions with relatively small kernel sizes produced a

cleaner heatmap than having fewer layers with larger kernels. In the end, a CNN with five convolutional layers gave the cleanest heatmap with the most contrast between rock glaciers and other classes. Our final CNN had the architecture $3 \times 3 \times 70$, $7 \times 7 \times 40$, $3 \times 3 \times 20$, $1 \times 1 \times 12$, $3 \times 3 \times 12$ with max pooling applied to the third and fifth layers. The trained CNN model was then applied producing a predictive heatmap, with each pixel indicating the probability (ranging from 0 to 1 of rock glacier presence. The heatmap was then smoothed with a 7×7 Gaussian filter.

4.2.2. Pléiades imagery analysis

We repeated our analysis using the four Pléiades multispectral (Red, Green, Blue, NIR) bands at 2 m resolution for a subset of the Poiqu catchment. We chose to not use the 0.5 m pan-sharpened imagery due to the memory demands of processing at such a resolution. As the Pléiades satellite imagery does not include a shortwave infrared (SWIR) spectral band, the analysis had to be modified. This also meant that certain multispectral indices such as the MNDWI could not be included. Due to the finer resolution we however opted to include a canny edge detection filter on the slope raster in the analysis. The rest of the classification procedure was the same as for the Sentinel-2 imagery.

4.2.3. OBIA reshaping

The reshaping of image objects in order to create rock glacier outlines was also performed in eCognition. As is common with OBIA, parameters in the image segmentation as well as thresholds in the image classification were chosen subjectively (Hay and Castilla, 2008; Blaschke et al., 2014).

A three-level image segmentation was conducted based on the multispectral bands as well as the slope. We found that having a multi-level segmentation helped group rock glaciers into larger objects, thereby making the reshaping simpler to perform. The resulting objects were then classified using a combination of the mean deep learning heatmap, the morphology (mainly the slope, and the standard deviation of the slope which was used to gauge the surface roughness), object shape and contextuality. Details of the thresholds used are given in Fig. 3. Objects were classified as rock glaciers using a combination of fixed and fuzzy criteria. The resulting outlines were expanded using a pixel-based growing algorithm based on a 5×5 kernel. Objects were expanded if 50% of the kernel had a heatmap value greater than 0.3. This helped include more irregularly shaped parts of the rock glaciers, such as the sections next to the headwall of the mountain. Lastly, the outlines were smoothed using a 7×7 kernel pixel-based growing and shrinking algorithm before being exported as ESRI Shapefiles.

4.2.4. Accuracy assessment

Assessing the accuracy of remote sensing classifications can be troublesome and is heavily dependent on the quality of the validation data. For both study regions, RG_Man outlines were used based on orthorectified Pléiades imagery and accompanying DEM to map rock glaciers geomorphologically, following the criteria set out by Delaloye et al. (2019). A national rock glacier inventory exists for Chile (Dirección General de Aguas (DGA), 2012, Barcaza et al., 2017), however when we visually inspected the inventory there were several cases of over- and underestimates of rock glacier size and missing polygons. As such our accuracy assessment was exclusively based on the Pléiades derived outlines. We computed accuracies for the Sentinel-2 classifications over both catchments. An accuracy assessment was also performed for a subset of the Poiqu catchment using both Pléiades and Sentinel-2 imagery.

We determined accuracies in two ways. In both cases our accuracy assessment was based on the rock glacier outlines and rock glacier absence (i.e. clean ice, debris-covered glaciers, shadows, or stable terrain), The first method is a simplistic approach to quantifying classification accuracies based on the percentage overestimation or underestimation when compared to RG_Man. Many studies on automated glacier and rock glacier inventories use this method (for example Paul et al. (2004), Alifu et al. (2015), Mithan et al. (2019)). This however can be too simplistic, and neglects errors of omission and commission, which over larger areas can conceivably cancel each other out. As such we portioned our data into a training and validation set in which we determined errors of omission and commission; namely a user's accuracy (the percentage of the CNN_OBIA classification that is actually a rock glacier) and a producer's accuracy (the percentage of total rock glaciers that were classified by the CNN_OBIA method). Given that our analysis using the Pléiades data had a different extent to the catchment-scale analysis of Poiqu, we also computed accuracies for the Sentinel-2 analysis using the same extent as the Pléiades analysis to compare accuracies.

Many papers addressing machine learning on remote sensing imagery typically adopt cross-validation techniques (e.g. Brenning (2009), Brenning et al. (2012), Knevels et al. (2019)) which are less affected by spatial autocorrelation (Schratz et al., 2019). Cross-validation was difficult to implement within this study owing both to the computational challenges of re-running our analysis multiple times, as well as the OBIA refinement that we performed being based on subjective thresholds Our validation techniques are however in line with other studies that integrate CNN with OBIA (Csillik et al., 2018; Fu et al., 2019; Ghorbanzadeh et al., 2019; Zhang et al., 2020) although we do acknowledge that by not accounting for spatial autocorrelation, our accuracy assessment may be over-optimistic.

5. Results

For the validation data over both study sites, the CNN_OBIA classification mapped in total 108 rock glaciers (26.0 km^2) out of 120 (20.3 km^2) in RG_Man. This corresponds to an overestimation of 28.0% (Table 2). The user's and producer's accuracies were 65.9% and 71.4% respectively, indicating that a moderately high proportion of the total rock glacier was identified yet the classification contains false positives.

5.1. La Laguna catchment

When looking at the validation data, our CNN_OBIA detected 26 of the 39 rock glaciers with a mean size of 0.2 km^2 (Fig. 4). In total 4.42 km^2 out of 4.39 km^2 were detected, representing a mean

Table 2
Classification accuracies for the CNN_OBIA classification for the La Laguna catchment, Poiqu catchment and Poiqu catchment using Pléiades imagery based on the validation set of the data. Note that in order to assess the impact of using higher-resolution Pléiades imagery, we also present the accuracy of the Sentinel-2 classification for the same subset as the Pléiades analysis. The mean over/underestimation of total rock glacier area is shown for both catchments combined is also shown.

Classification	User accuracy (%)	Producer accuracy (%)	Over/Underestimation (%)
La Laguna	63.9	75.4	+0.6%
Poiqu	68.8	75.0	+43.6
Poiqu subset (Sentinel-2)	62.9	87.4	99.2
Poiqu subset (Pléiades)	72.0	88.4	+23.2
Total (Sentinel)	65.9	71.4	+28.0

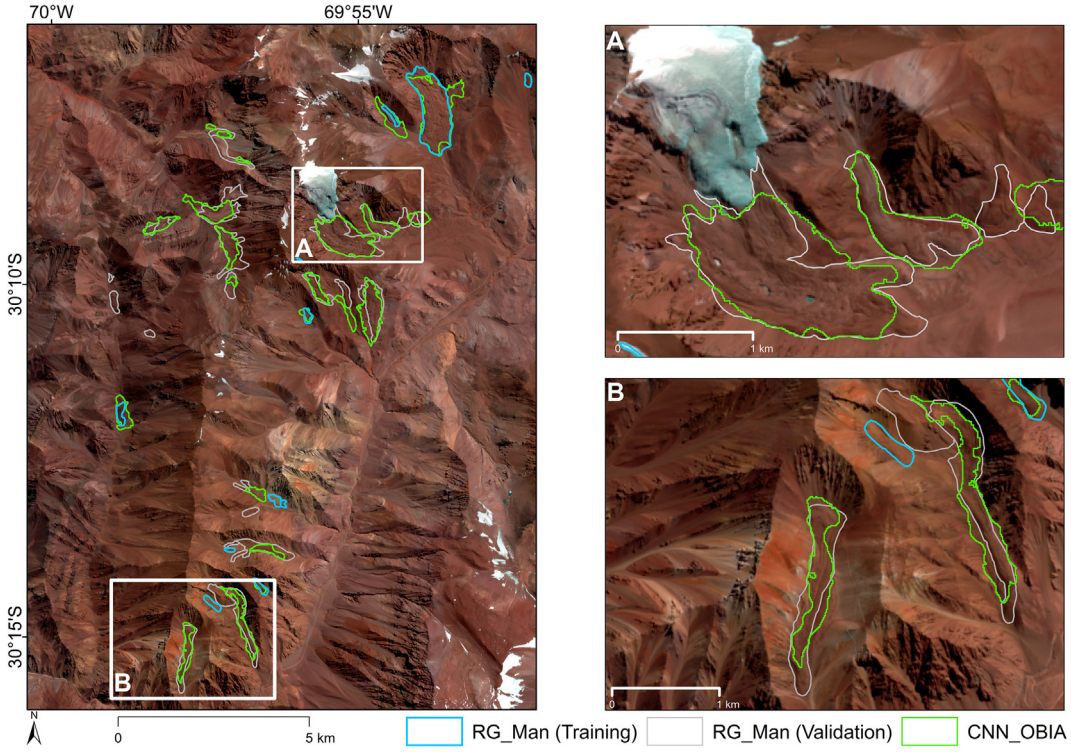

Fig. 4. Comparison of automatically generated rock glacier outlines (CNN_OBIA) with the manually corrected outlines (RG_Man) for the La Laguna catchment. Polygons used for training and validation are shown. The background image is a false colour Sentinel-2 dataset from 04/04/2018.

overestimation of 0.6%. Of those detected, the three largest landforms are rock glaciers CL104300054 (1.50 km^2), CL104300039 (Tapado rock glacier; 1.01 km^2), and CL104300038 (0.63 km^2). Rock glaciers were detected at elevations ranging from 3814 to 4948 m a.s.l. Individual estimations of rock glacier area range considerably. Generally larger rock glaciers were classified with lower classification errors, with glaciers between 0.1 and 0.2 km^2 being on average underestimated by 6.8%, while rock glaciers less than 0.1 km^2 in area were overestimated by an average of 115.9%. We determined a user's accuracy of 63.9% and a producer's accuracy of 75.4%.

5.2. Poiqu catchment

When compared to the validation data, CNN_OBIA mapped 82 rock glaciers (18.0 km^2) out of 90 (12.5 km^2) resulting in an overestimation of the area by 43.6% (Fig. 5). There was a large variability of over- and underestimations between individual rock glacier polygons, from rock glaciers that were underestimated by > 90% to those that were vastly overestimated by more than 450%, although it should be noted that these rock glacier polygons were generally the smallest found in the RG_Man inventory. Generally, the smallest rock glaciers (< 0.05 km^2) were mapped with the lowest accuracies (overestimations of 207.5%). The magnitude of error decreased as the mean rock glacier area increased, with rock glaciers between 0.2 and 0.3 km^2 being underestimated by an average of 42.8%, while rock glaciers with areas between 0.3 and 0.5 km^2 were underestimated by 11.3%. The largest rock glaciers in the region however were overestimated by 37.4%. The user's accuracy was 68.9% indicating that the classification contained false positives within the classification. The producer's accuracy was 75.0% with a user's accuracy of 56.5%.

5.2.1. Pléiades imagery classification

The validation data for the portion of the Poiqu catchment that was classified with the Pléiades imagery contained seven rock glaciers totalling 2.1 km^2. Of these the CNN_OBIA_Ple classification identified all seven rock glaciers (total area 2.6 km^2) with an overestimation of rock glacier area of 23.2%, as visible in Fig. 6. It seems that three rock glacier outlines were misclassified and grouped as a single polygon (Fig. 6). The misclassified landforms has a morphology that is similar to the rock glaciers, causing a high probability heatmap score resulting in CNN_OBIA_Ple grouping the landforms as one. It can be difficult to reliably determine from the satellite imagery if these landforms are periglacial, glacial or fluvial in nature When evaluating the influence of running the classification on Pléiades imagery instead of Sentinel-2 imagery, we found that the producer accuracy remains approximately the same (87.4% with Sentinel-2, 88.4% with Pléiades), however the user accuracy increases with the use of higher-resolution imagery (62.9% with Sentinel-2, 72.0% for Pléiades).When comparing the rock glaciers found in the validation data for both classifications, CNN_OBIA_Ple outperformed CNN_OBIA on 3 polygons, was equivalent on 1 polygon, and performed worse on 2 polygons. The rock glaciers on the southern slope of the Mulaco massif were generally delineated with higher accuracies (74.4%) than those on the northern slopes (44.4%).

6. Discussion

6.1. Use of deep learning to classify rock glaciers

On average, our CNN_OBIA classification managed to map rock glaciers in two distinct periglacial environments with a mean overestimation of 28%. The user accuracy ranges from 63.9 to 68.9% indicating that the final classified polygons included false positives that were not rock glaciers. The producer accuracies were 75.4% and 75.0% for the La Laguna and Poiqu catchments respectively, indicating that even although the individual rock glacier polygons were in most cases overestimated, a large proportion of the total rock glaciers were successfully identified. The CNN itself is only capable of identifying features large enough to be detected after the convolution. In our case, we convolved our image five times and applyied max pooling twice to reduce noise, meaning that a rock glacier approximately 30 × 30 pixels

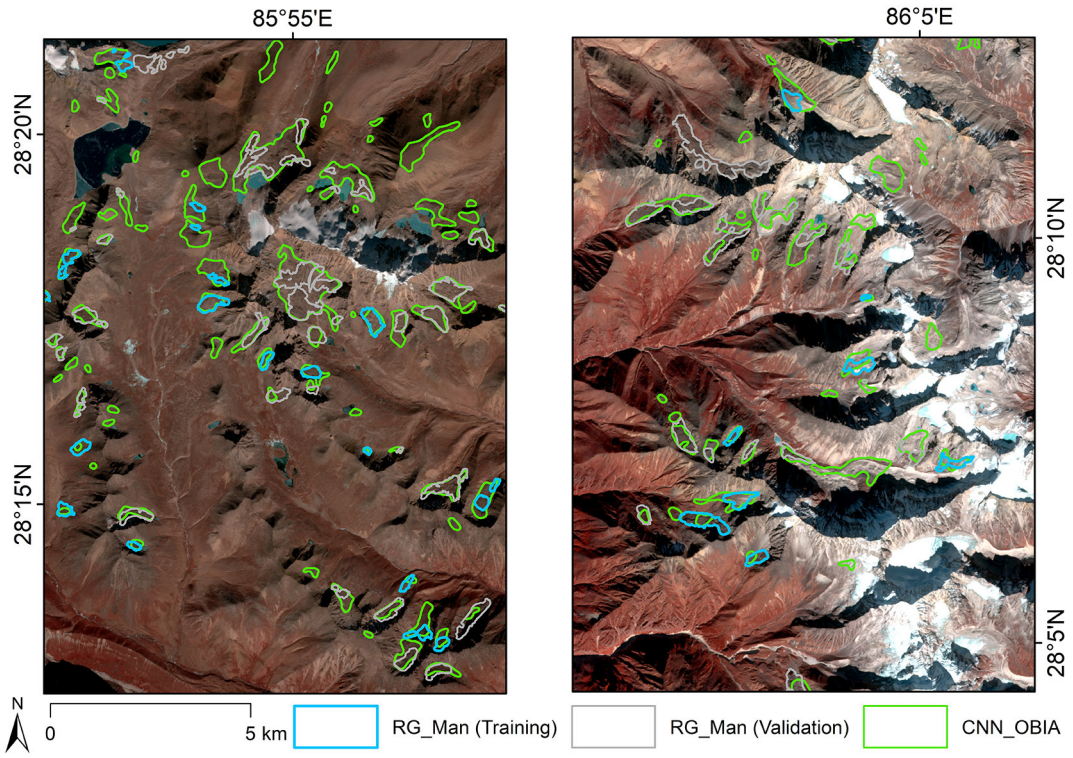

Fig. 5. Comparison of automatically generated rock glacier outlines (CNN_OBIA) with the manually corrected outlines (RG_Man) for the Poiqu catchment. Polygons used for training and validation are shown. The background image is a false colour Sentinel-2 dataset from 09/12/2016.

in size (300 × 300 m) would be visible as 3 × 3 (30 × 30 m) pixels on the generated heatmap, which is below the 0.025 km^2 (i.e. 158 × 158 m) threshold used in the OBIA refinement. As such, due to the finer spatial resolution the Pléiades classification was able to classify much smaller landforms with more subtle, smaller-scale morphological patterns that were not visible on the Sentinel-2 imagery. The higher producer's accuracy of CNN_OBIA_Ple therefore suggests that higher resolution satellite imagery is more suitable for identifying smaller rock glaciers, or rock glaciers with less prominent surface features.

While our method worked well in both of our study catchments, the flexible nature of machine learning methods, such as CNNs, means we cannot be certain that our method will work equally well in other periglacial catchments.

The probability heatmap corresponds well with RG_Man and it appears that the heatmap value relates to the prominence of the surface morphology, with landforms exhibiting marked morphology such as ridges and furrows (for example Fig. 7A) having higher probability heatmap values than those areas without prominent morphology (for example Fig. 7B). This infers that our method is more suitable for identifying active rock glaciers with prominent surface morphology.

The heatmap produced from the deep learning itself could be used as auxiliary data to aid the creation of rock glacier inventories. Our CNN_OBIA method could be used to reduce the uncertainty associated with manual inventories due to inter-user inconsistencies and personal subjectivity. Our method could provide a rock glacier outline base product which could be refined manually to create a finalised rock glacier inventory, thereby reducing the amount of manual digitisation required.

6.2. Comparison with other rock glacier inventory methods

The majority of rock glacier inventories are compiled with manual interpretation of high-resolution imagery, often complimented with auxiliary data (morphological or kinematic) (e.g. Villarroel et al. (2018), Bolch et al. (2019)). It is not straightforward to compare these classifications to ours, as in the absence of reference data these studies do not provide accuracy assessments. Additionally, the scale of analysis differs, some of the rock glacier inventories created manually have been conducted over regional scales (for example Wang et al., 2017; Villarroel et al., 2018) compared to our catchment scale. We can however compare the strengths and weaknesses of the methods involved.

The most common recent form of auxiliary data used in the creation of rock glacier inventories is surface velocities or kinematics derived from SAR interferometry (Liu et al., 2013; Bodin et al., 2016; Wang et al., 2017; Villarroel et al., 2018). Our CNN_OBIA method has a couple of key advantages over the use of interferometry. Firstly, it is possible to identify inactive rock glaciers which would not be identified using velocities alone since they are essentially not flowing. These features however are still important for the local hydrology and are a physical manifestation of permafrost. Additionally, our CNN_OBIA method is not reliant on VHR and costly satellite imagery, and instead runs on freely available 10 m resolution Sentinel-2 imagery. In our case we produced a DEM from commercial stereo imagery, however many regions of the world are covered by freely available DEMs of comparable resolutions. Unlike interferometry, our CNN_OBIA method is not restricted to analysing rock glaciers that are oriented in the LOS of the satellite, is less influenced by atmospheric disturbances, and does not depend on maintaining high SAR coherence between multiple acquisitions. This latter point means that the CNN_OBIA methodology can be equally be applied to regions where vegetation is growing either within the vicinity of rock glaciers, or on the rock glaciers themselves, providing a solution to the problem encountered by Bertone et al. (2019) when working in the Italian Alps. Finally, DInSAR is dependent on the perpendicular and temporal baselines making it easier to calculate over a larger area, whereas the CNN_OBIA method does not have this limitation.

Our method builds on the work of Brenning et al. (2012) who used textural filters on IKONOS imagery to identify rock glaciers based on

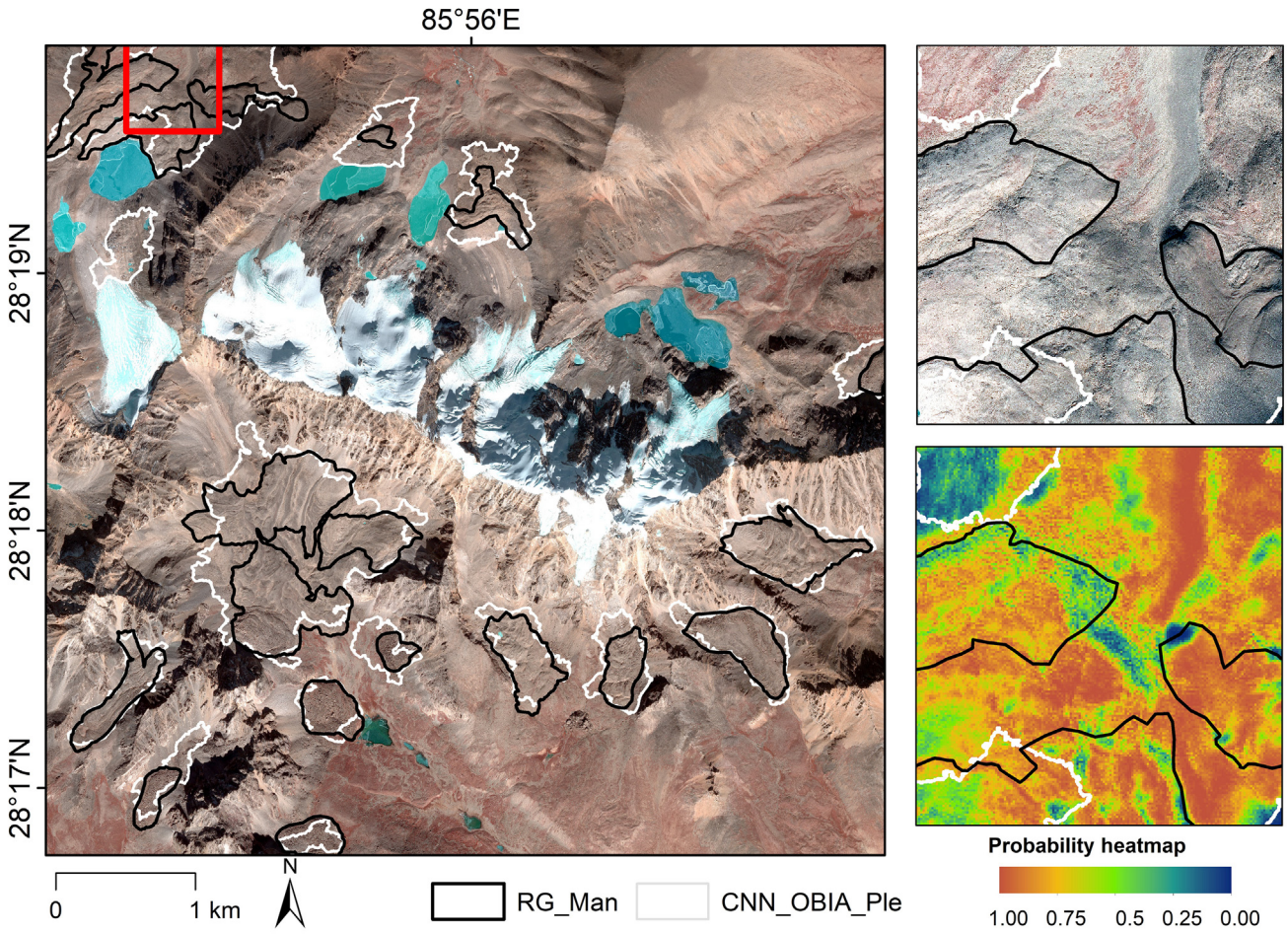

Fig. 6. Comparison of automatically generated rock glacier outlines based on the Pléiades imagery. (CNN_OBIA_Ple) with the manually corrected outlines (RG_Man) for a subset of the Poiqu catchment. The panels on the right show a subset of the area (shown with a red outline on the left panel) that was misclassified (upper) along with the corresponding probability heatmap (lower). Background imagery shows orthorectified Pléiades imagery © CNES (2018), and Airbus DS (2018), all rights reserved.

surface morphology indicative of flow patterns It is not possible to compare accuracies due to differences in validation (computation of AUROC (Area Under the Receiver Operating Characteristic) as well as masking of areas by topography, bedrock, and landcover). Importantly though, our method was applied using freely available Sentinel-2 imagery available worldwide. As such we believe that analysis of textural signatures shows promise for identifying rock glaciers.

Our method is however not without limitations. One shortcoming is that sufficient and reliable inventory data must be available for a given region in order to train the CNN model. The training data does not need to be spatially complete, but nevertheless this can be challenging for completely unstudied periglacial regions. Secondly, since the CNN relies on identifying recurring spectral patterns and textures, it can misclassify debris flows, rock avalanche deposits and fluvial environments as rock glaciers which share some spectral, textural and morphological properties. This was problematic for both the Sentinel-2 classification and the Pléiades classification. The OBIA reshaping however helps mitigate these false positives to an extent, in a way that cannot be achieved solely using CNNs. OBIA allows objects to be excluded that are irregularly shaped, or by their spectral or morphological properties. As such, while the raw probability heatmap can assist an analyst to identify rock glaciers manually, by running the whole procedure through OBIA, it is possible to segment the imagery and obtain individual rock glacier polygons in an automated way.

6.3. Potential methodological developments

Our method shows promise yet there further development is needed before the method can be used to create rock glacier inventories over large areas without significant manual editing. At present, our method is prone to misclassifying landforms with similar textural characteristics such as rock avalanche deposits. However, these landforms can also be visually difficult to distinguish from rock glaciers without additional information. One possible solution to this could be including surface velocity data, either derived from feature tracking or from SAR interferometry, albeit with the limitation of LOS movements as discussed earlier. This would have the additional advantage of being able to classify rock glaciers based on their level of activity and would likely reduce the number of false positives in the classification. Using a combination of CNNs and OBIA could also be useful for other landforms that are hard to identify using image spectra alone, such as debris-covered glaciers, lava flows, and landslides.

7. Conclusion

Studies of rock glaciers over catchment to regional scales are hampered by inventories of variable quality that are based on subjective criteria and prone to inter-user inconsistencies. In this study we have presented a semi-automated workflow to map rock glaciers based on freely available Sentinel data and a high-resolution DEM using a

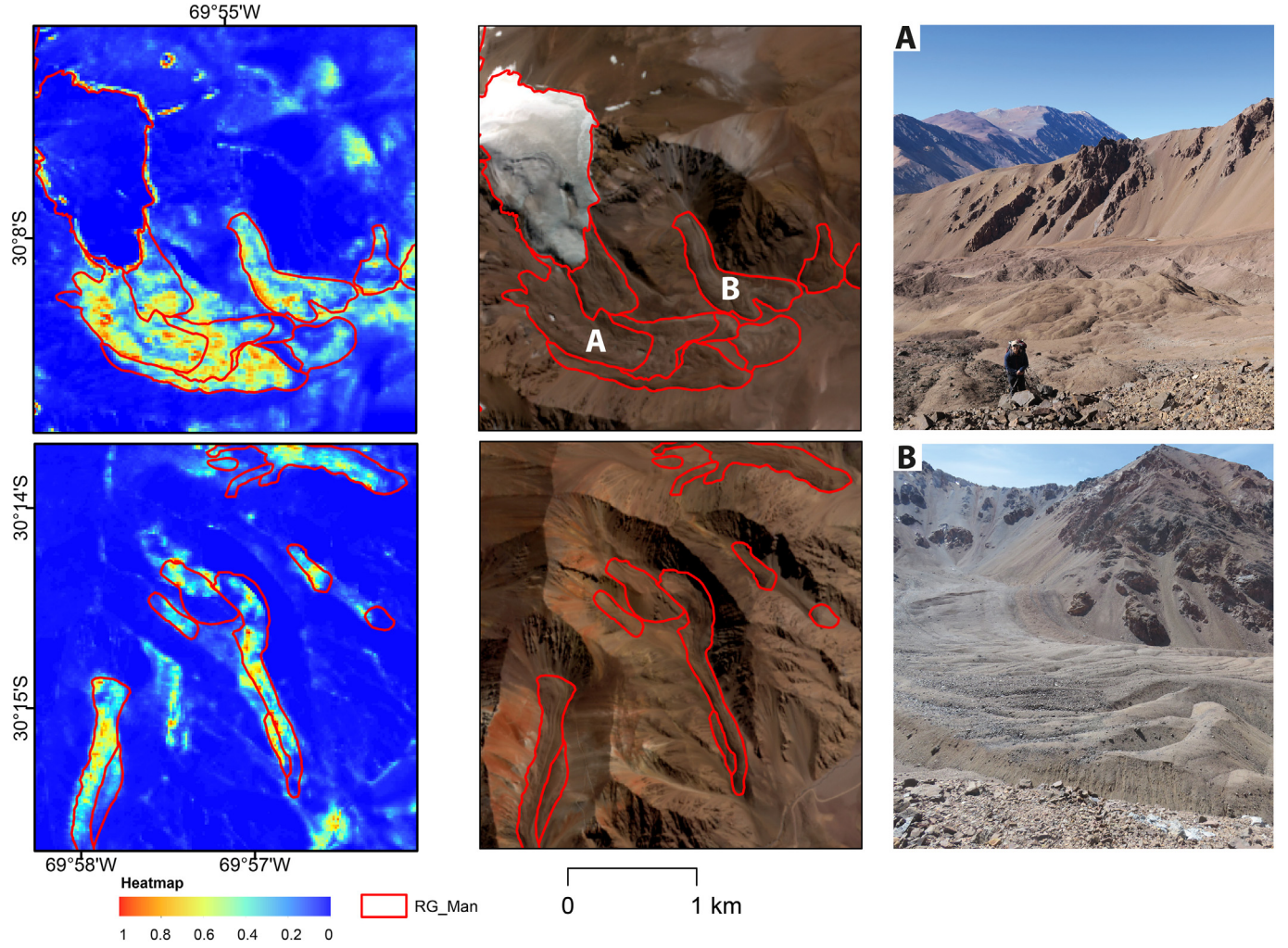

Fig. 7. Comparison between the deep learning heatmap for two areas within the La Laguna catchment (left) with RG_Man rock glacier outlines overlying Sentinel-2 imagery (centre). The right panel shows two field photographxs taken in March 2019 of the surface of Tapado glacier complex (A) and Las Tolas rock glacier (B).

combination of CNNs and OBIA. We trialled our method in two catchments, the La Laguna catchment in the semi-arid Andes of Chile, and the Poiqu catchment in central Himalaya. Our method managed to map rock glaciers across both catchments with a mean overestimation of 28.0% with the freely available remote sensing data. Producer accuracies were higher than user accuracies indicating that the classification successfully identified many of the rock glaciers in each catchment, yet the rock glacier outlines created contained false positives that must be removed manually. We found that better detection rates are not necessarily obtained from using VHR Pléiades satellite data, although the rock glaciers identified are mapped with a higher user accuracy. There are also some limitations with texturally similar landforms such as debris flows, avalanches, and fluvial deposits that become misclassified as rock glaciers. Nevertheless, our method produced promising results, runs as one workflow, and reduces the amount of manual work required. Further advances in machine learning methods are likely to lead to refined identification of rock glacier surface textures, as such we recommend the continued use of deep learning to semi-automatically identify rock glaciers and believe that OBIA provides a good framework for conducting and further automating the analysis.

Description of author's responsibilities

The study was conceptualised by BAR, TB, SM and PR. The analysis was performed by BAR and DH. All authors contributed to writing and editing the manuscript.

Dedication

This article is dedicated in memory of Michael Williams (1956 - 2020).

Declaration of Competing Interest

The authors declare that they have no known competing financial interests or personal relationships that could have appeared to influence the work reported in this paper.

Acknowledgements

B Robson was supported by the Meltzer foundation and a University of Bergen grant. S MacDonell was supported by CONICYT-Programa Regional (R16A10003) and the Coquimbo Regional Government via FIC-R(2016)BIP 40000343. D. Hölbling has been supported by the Austrian Science Fund through the project MORPH (Mapping, Monitoring and Modeling the Spatio-Temporal Dynamics of Land Surface Morphology; FWF-P29461-N29). N Schaffer was financed by CONICYT-FONDECYT (3180417) and P Rastner by the ESA Dragon 4 programme (4000121469/17/I-NB). Thank you to Anna Telegina who

read an early version of the manuscript. We are thankful to ESA for the provision of Sentinel data and CNES/Airbus DS for the provision of the Pléiades satellite data for a reduced price within the ISIS programme. We are grateful for the constructive comments from three anonymous reviewers.

Appendix A. Supplementary data

Supplementary data to this article can be found online at https://doi.org/10.1016/j.rse.2020.112033.

References

Alba, M., Barazzetti, L., Scaioni, M., Remondino, F., 2011. Automatic registration of multiple laser scans using panoramic RGB and intensity images. Int. Arch. Photogramm. Remote. Sens. Spat. Inf. Sci. 3812, 49–54.

Alifu, H., Tateishi, R., Johnson, B., 2015. A new band ratio technique for mapping debris-covered glaciers using Landsat imagery and a digital elevation model. Int. J. Remote Sens. 36, 2063–2075.

Azocar, G.F., Brenning, A., 2010. Hydrological and geomorphological significance of rock glaciers in the dry Andes, (27 degrees-33 degrees S). Permafr. Periglac. Process. 21, 42–53.

Barboux, C., Delaloye, R., Lambiel, C., 2014. Inventorying slope movements in an Alpine environment using DInSAR. Earth Surf. Process. Landf. 39, 2087–2099.

Barcaza, G., Nussbaumer, S.U., Tapia, G., Valdés, J., García, J.L., Videla, Y., Albornoz, A., Arias, V., 2017. Glacier inventory and recent glacier variations in the Andes of Chile, South America. Ann. Glaciol. 58 (75pt2), 166–180.

Barsch, D., 1996. Rock Glaciers. Springer, Berlin.

Bentes, C., Frost, A., Velotto, D., Tings, B., 2016. Ship-iceberg discrimination with convolutional neural networks in high resolution SAR images. In: Proceedings of EUSAR 2016: 11th European Conference on Synthetic Aperture Radar. VDE, pp. 1–4.

Bertone, A., Zucca, F., Marin, C., Notarnicola, C., Cuozzo, G., Krainer, K., Mair, V., Riccardi, P., Callegari, M., Seppi, R., 2019. An unsupervised method to detect rock glacier activity by using Sentinel-1 SAR interferometric coherence: a regional-scale study in the Eastern European Alps. Remote Sens. 11 (14), 1711.

Bianchi, F.M., Grahn, J., Eckerstorfer, M., Malnes, E., Vickers, H.J.A.P.A., 2019. Snow avalanche segmentation in SAR images with fully convolutional neural networks. arXiv preprint arXiv 1910, 05411.

Blaschke, T., Hay, G.J., Kelly, M., Lang, S., Hofmann, P., Addink, E., Feitosa, R.Q., Van Der Meer, F., Van Der Werff, H., Van Coillie, F., 2014. Geographic object-based image analysis–towards a new paradigm. ISPRS J. Photogramm. Remote Sens. 87, 180–191.

Bodin, X., Thomas, E., Liaudat, D.T., Vivero, S., Pitte, P., 2016. Rock Glacier Activity and Distribution in the Semi-Arid Andes of Chile and Argentina Detected from dInSAR. Proceedings of the International Conference on Permafrost, Potsdam, Germany, pp. 20–24.

Bolch, T., Gorbunov, A.P., 2014. Characteristics and origin of rock glaciers in Northern Tien Shan (Kazakhstan/Kyrgyzstan). Permafr. Periglac. Process. 25, 320–332.

Bolch, T., Marchenko, S. (Eds.), 2009. Significance of Glaciers, Rock Glaciers and Ice-Rich Permafrost in the Northern Tien Shan as Water Towers under Climate Change Conditions. IHP/HWRP-Berichte, Almaty, Kazakhstan vols. 28-30 Nov. 2006.

Bolch, T., Buchroithner, M.F., Kunert, A., Kamp, U., 2007. Automated delineation of debris-covered glaciers based on ASTER data. Geoinformation in Europe. In: Proceedings of the 27th EARSeL Symposium, pp. 4–6.

Bolch, T., Rohrbach, N., Kutuzov, S., Robson, B., Osmonov, A., 2019. Occurrence, evolution and ice content of ice-debris complexes in the Ak-Shiirak, central Tien Shan revealed by geophysical and remotely-sensed investigations. Earth Surf. Process. Landf. 44, 129–143.

Bolch, T., Rastner, P., Pronk, J.B., Bhattacharya, A., Liu, L., Hu, Y., Zhang, G.Q., Yao, T.D., 2020. Occurrence and characteristics of Ice-Debris landforms in Poiqu Basin – Central Himalaya. In: EGU General Assembly 2020. Geophysical Research Abstracts, Vienna, Austria.

Brardinoni, F., Scotti, R., Sailer, R., Mair, V., 2019. Evaluating sources of uncertainty and variability in rock glacier inventories. Earth Surf. Process. Landf. 44 (12), 2450–2466.

Brenning, A., 2009. Benchmarking classifiers to optimally integrate terrain analysis and multispectral remote sensing in automatic rock glacier detection. Remote Sens. Environ. 113, 239–247.

Brenning, A., Long, S.L., Fieguth, P., 2012. Detecting rock glacier flow structures using Gabor filters and IKONOS imagery. Remote Sens. Environ. 125, 227–237.

Colucci, R.R., Forte, E., Žebre, M., Maset, E., Zanettini, C., Guglielmin, M., 2019. Is that a relict rock glacier? Geomorphology 330, 177–189.

Cremonese, E., Gruber, S., Phillips, M., Pogliotti, P., Böckli, L., Noetzli, J., Suter, C., Bodin, X., Crepaz, A., Kellerer-Pirklbauer, A., 2011. An inventory of permafrost evidence for the European Alps. Cryosphere 5, 651–657.

Csillik, O., Cherbini, J., Johnson, R., Lyons, A., Kelly, M., 2018. Identification of citrus trees from unmanned aerial vehicle imagery using convolutional neural networks. Drones 2.

Dao, P., Liou, Y.-A., 2015. Object-based flood mapping and affected rice field estimation with Landsat 8 OLI and MODIS data. Remote Sens. 7, 5077–5097.

Delaloye, R., Barboux, C., Echelard, T., Bodin, X., Brardinoni, F., Lambiel, C., Wee, J., 2019. Towards standard guidelines for inventorying rock glaciers (version 2.0). In: IPA Action Group Rock Glacier Inventories and Kinematics (2018–2020), (Available Online: unifr.ch/geo/geomorphology/en/research/ipa-action-group-rock-glacier/).

Ding, A., Zhang, Q., Zhou, X., Dai, B., 2016. Automatic recognition of landslide based on CNN and texture change detection. In: 2016 31st Youth Academic Annual Conference of Chinese Association of Automation (YAC). 2016. pp. 444–448 11–13 November.

Dirección General de Aguas (DGA), 2012. Chilean National Glacier Inventory. (unpublished data).

Drăguţ, L., Csillik, O., Eisank, C., Tiede, D., 2014. Automated parameterisation for multi-scale image segmentation on multiple layers. ISPRS J. Photogramm. Remote Sens. 88, 119–127.

Esper Angillieri, M.Y., 2009. A preliminary inventory of rock glaciers at 30°S latitude, cordillera frontal of San Juan, Argentina. Quat. Int. 195, 151–157.

Falaschi, D., Castro, M., Masiokas, M., Tadono, T., Ahumada, A.L., 2014. Rock glacier inventory of the Valles Calchaquíes region (~ 25 S), Salta, Argentina, derived from ALOS data. Permafr. Periglac. Process. 25, 69–75.

Favier, V., Falvey, M., Rabatel, A., Praderio, E., López, D., 2009. Interpreting discrepancies between discharge and precipitation in high-altitude area of Chile's Norte Chico region (26–32°S). Water Resour. Res. 45.

Fu, Y., Liu, K., Shen, Z., Deng, J., Gan, M., Liu, X., Lu, D., Wang, K., 2019. Mapping impervious surfaces in town–rural transition belts using China's GF-2 imagery and object-based deep CNNs. Remote Sens. 11, 280.

Gallego, A.J., Pertusa, A., Gil, P., 2018. Automatic ship classification from optical aerial images with convolutional neural networks. Remote Sens. 10, 511.

Geiger, S.T., Daniels, J.M., Miller, S.N., Nicholas, J.W., 2014. Influence of rock glaciers on stream hydrology in the La Sal Mountains, Utah. Arct. Antarct. Alp. Res. 46, 645–658.

Ghorbanzadeh, O., Blaschke, T., Gholamnia, K., Meena, S.R., Tiede, D., Aryal, J., 2019. Evaluation of different machine learning methods and deep-learning convolutional neural networks for landslide detection. Remote Sens. 11, 196.

González-Audícana, M., Otazu, X., Fors, O., Seco, A., 2005. Comparison between Mallat's and the 'à trous' discrete wavelet transform based algorithms for the fusion of multispectral and panchromatic images. Int. J. Remote Sens. 26, 595–614.

Gorbunov, A., Titkov, S., 1989. Kamennye Gletchery Gor Srednej Azii (Rock Glaciers of the Central Asian Mountains). Akademia Nauk SSSR, Irkutsk.

Guirado, E., Tabik, S., Alcaraz-Segura, D., Cabello, J., Herrera, F., 2017. Deep-learning versus OBIA for scattered shrub detection with Google earth imagery: *Ziziphus lotus* as case study. Remote Sens. 9, 1220.

Haeberli, W., Hallet, B., Arenson, L., Elconin, R., Humlum, O., Kääb, A., Kaufmann, V., Ladanyi, B., Matsuoka, N., Springman, S., 2006. Permafrost creep and rock glacier dynamics. Permafr. Periglac. Process. 17, 189–214.

Hay, G.J., Castilla, G., 2008. Geographic Object-Based Image Analysis (GEOBIA): a new name for a new discipline. In: Blaschke, T., Lang, S., Hay, G.J. (Eds.), Object-Based Image Analysis: Spatial Concepts for Knowledge-Driven Remote Sensing Applications. Springer Berlin Heidelberg, Berlin, Heidelberg.

Hirschmuller, H., 2007. Stereo processing by semiglobal matching and mutual information. IEEE Trans. Pattern Anal. Mach. Intell. 30, 328–341.

Hölbling, D., Füreder, P., Antolini, F., Cigna, F., Casagli, N., Lang, S., 2012. A semi-automated object-based approach for landslidedetection validated by persistent scatterer interferometry measures and landslide inventories. Remote Sens. 4, 1310–1336.

Hölbling, D., Betts, H., Spiekermann, R., Phillips, C., 2016. Identifying spatio-temporal landslide hotspots on North Island, New Zealand, by analyzing historical and recent aerial photography. Geosciences 6, 48.

Huang, L., Luo, J., Lin, Z., Niu, F., Liu, L., 2020. Using deep learning to map retrogressive thaw slumps in the Beiluhe region (Tibetan plateau) from CubeSat images. Remote Sens. Environ. 237, 111534.

Huggel, C., Allen, S., Wymann Von Dach, S., Dimri, A.P., Mal, S., Linbauer, A., Salzmann, N., Bolch, T., 2020. An integrative and joint approach to climate impacts, hydrological risks and adaptation in the Indian Himalayan region. In: Himalayan Weather and Climate and their Impact on the Environment. Springer International Publishing, pp. 553–573.

Huss, M., Hock, R., 2018. Global-scale hydrological response to future glacier mass loss. Nat. Clim. Chang. 8 (2), 135–140.

Immerzeel, W.W., Van Beek, L.P.H., Bierkens, M.F.P., 2010. Climate change will affect the Asian water towers. Science 328, 1382–1385.

Janke, J.R., 2001. Rock glacier mapping: a method utilizing enhanced TM data and GIS modeling techniques. Geocarto Int. 16, 5–15.

Jones, D., Harrison, S., Anderson, K., Betts, R., 2018a. Mountain rock glaciers contain globally significant water stores. Sci. Rep. 8, 2834.

Jones, D., Harrison, S., Anderson, K., Selley, H., Wood, J., Betts, R., 2018b. The distribution and hydrological significance of rock glaciers in the Nepalese Himalaya. Glob. Planet. Chang. 160, 123–142.

Jozdani, S., Chen, D., 2020. On the versatility of popular and recently proposed supervised evaluation metrics for segmentation quality of remotely sensed images: an experimental case study of building extraction. ISPRS J. Photogramm. Remote Sens. 160, 275–290.

Kääb, A., Vollmer, M., 2000. Surface geometry, thickness changes and flow fields on creeping mountain permafrost: automatic extraction by digital image analysis. Permafr. Periglac. Process. 11 (4), 315–326.

Kehrwald, N.M., Thompson, L.G., Yao, T.D., Mosley-Thompson, E., Schotterer, U., Alfimov, V., Beer, J., Eikenberg, J., Davis, M.E., 2008. Mass loss on Himalayan glacier endangers water resources. Geophys. Res. Lett. 35.

Knevels, R., Petschko, H., Leopold, P., Brenning, A., 2019. Geographic object-based image analysis for automated landslide detection using open source GIS software. ISPRS Int. J. Geo Inf. 8 (12), 551.

Kofler, C., Steger, S., Mair, V., Zebisch, M., Comiti, F., Schneiderbauer, S., 2019. An inventory-driven rock glacier status model (intact vs. relict) for South Tyrol, Eastern Italian Alps. Geomorphology 106887.

Lang, S., 2008. Object-based image analysis for remote sensing applications: modeling reality–dealing with complexity. In: Object-Based Image Analysis. Springer, Berlin,

Heidelberg, pp. 3–27.
Längkvist, M., Kiselev, A., Alirezaie, M., Loutfi, A., 2016. Classification and segmentation of satellite orthoimagery using convolutional neural networks. Remote Sens. 8, 329.
Li, Y., Zhang, H., Xue, X., Jiang, Y., Shen, Q., 2018. Deep learning for remote sensing image classification: a survey. Wiley Interdisc. Rev. Data Min. Knowl. Discov. 8, e1264.
Liu, L., Millar, C.I., Westfall, R.D., Zebker, H.A., 2013. Surface motion of active rock glaciers in the Sierra Nevada, California, USA: inventory and a case study using InSAR. Cryosphere 7, 1109–1119.
Ma, L., Liu, Y., Zhang, X., Ye, Y., Yin, G., Johnson, B.A., 2019. Deep learning in remote sensing applications: a meta-analysis and review. ISPRS J. Photogramm. Remote Sens. 152, 166–177.
Mahdianpari, M., Salehi, B., Rezaee, M., Mohammadimanesh, F., Zhang, Y., 2018. Very deep convolutional neural networks for complex land cover mapping using multispectral remote sensing imagery. Remote Sens. 10, 1119.
Mallinis, G., Gitas, I.Z., Giannakopoulos, V., Maris, F., Tsakiri-Strati, M., 2013. An object-based approach for flood area delineation in a transboundary area using ENVISAT ASAR and LANDSAT TM data. Int. J. Digit. Earth 6, 124–136.
Mithan, H.T., Hales, T.C., Cleall, P.J., 2019. Supervised classification of landforms in Arctic mountains. Permafr. Periglac. Process. 30 (3), 131–145.
Monnier, S., Kinnard, C., Surazakov, A., Bossy, W., 2014. Geomorphology, internal structure, and successive development of a glacier foreland in the semiarid Chilean Andes (Cerro Tapado, upper Elqui Valley, 30°08′ S., 69°55′ W.). Geomorphology 207, 126–140.
Necsoiu, M., Onaca, A., Wigginton, S., Urdea, P., 2016. Rock glacier dynamics in Southern Carpathian Mountains from high-resolution optical and multi-temporal SAR satellite imagery. Remote Sens. Environ. 177, 21–36.
Nicholson, L., Marín, J., Lopez, D., Rabatel, A., Bown, F., Rivera, A., 2009. Glacier inventory of the upper Huasco valley, Norte Chico, Chile: glacier characteristics, glacier change and comparison with Central Chile. Ann. Glaciol. 50 (53), 111–118.
Onaca, A., Ardelean, F., Urdea, P., Magori, B., 2017. Southern Carpathian rock glaciers: inventory, distribution and environmental controlling factors. Geomorphology 293, 391–404.
Outcalt, S.I., Benedict, J.B.J., G, J.O., 1965. Photo-interpretation of two types of rock glacier in the Colorado front range, USA. J. Glaciol. 5 (42), 849–856.
Pandey, P., 2019. Inventory of rock glaciers in Himachal Himalaya, India using high-resolution google earth imagery. Geomorphology 340, 103–115.
Paul, F., Huggel, C., Kaab, A., 2004. Combining satellite multispectral image data and a digital elevation model for mapping debris-covered glaciers. Remote Sens. Environ. 89, 510–518.
Paul, F., Barrand, N.E., Baumann, S., Berthier, E., Bolch, T., Casey, K., Frey, H., Joshi, S., Konovalov, V., Le Bris, R., 2013. On the accuracy of glacier outlines derived from remote-sensing data. Ann. Glaciol. 54, 171–182.
Paul, F., Bolch, T., Kääb, A., Nagler, T., Nuth, C., Scharrer, K., Shepherd, A., Strozzi, T., Ticconi, F., Bhambri, R., 2015. The glaciers climate change initiative: methods for creating glacier area, elevation change and velocity products. Remote Sens. Environ. 162, 408–426.
Pfeffer, W.T., Arendt, A.A., Bliss, A., Bolch, T., Cogley, J.G., Gardner, A.S., Hagen, J.-O., Hock, R., Kaser, G., Kienholz, C., 2014. The Randolph glacier inventory: a globally complete inventory of glaciers. J. Glaciol. 60, 537–552.
Piao, S., Ciais, P., Huang, Y., Shen, Z., Peng, S., Li, J., Zhou, L., Liu, H., Ma, Y., Ding, Y., 2010. The impacts of climate change on water resources and agriculture in China. Nature 467 (7311), 43–51.
Pope, A., Rees, W.G., 2014. Impact of spatial, spectral, and radiometric properties of multispectral imagers on glacier surface classification. Remote Sens. Environ. 141, 1–13.
Pourrier, J., Jourde, H., Kinnard, C., Gascoin, S., Monnier, S., 2014. Glacier meltwater flow paths and storage in a geomorphologically complex glacial foreland: the case of the Tapado glacier, dry Andes of Chile (30°S). J. Hydrol. 519, 1068–1083.
Pritchard, H.D., 2019. Asia's shrinking glaciers protect large populations from drought stress. Nature 569, 649–654.
Racoviteanu, A., Williams, M.W., 2012. Decision tree and texture analysis for mapping debris-covered glaciers in the Kangchenjunga area, Eastern Himalaya. Remote Sens. 4, 3078–3109.
Rangecroft, S., Harrison, S., Anderson, K., Magrath, J., Castel, A.P., Pacheco, P., 2014. A first rock glacier inventory for the Bolivian Andes. Permafr. Periglac. Process. 25, 333–343.
Rangecroft, S., Harrison, S., Anderson, K., 2015. Rock glaciers as water stores in the Bolivian Andes: an assessment of their hydrological importance. Arct. Antarct. Alp. Res. 47, 89–98.
Rastner, P., Bolch, T., Notarnicola, C., Paul, F., 2013. A comparison of pixel-and object-based glacier classification with optical satellite images. IEEE J. Sel. Top. Appl. Earth Obs. Remote Sens. 7, 853–862.
Robson, B.A., Nuth, C., Dahl, S.O., Hölbling, D., Strozzi, T., Nielsen, P.R., 2015. Automated classification of debris-covered glaciers combining optical, SAR and topographic data in an object-based environment. Remote Sens. Environ. 170, 372–387.
Schaffer, N., Macdonell, S., 2020. Rock Glacier Inventory for the La Laguna Catchment (Unpublished Dataset). CEAZA, La Serena, Chile.
Schaffer, N., Macdonell, S., Réveillet, M., Yáñez, E., Valois, R., 2019. Rock glaciers as a water resource in a changing climate in the semiarid Chilean Andes. Reg. Environ. Chang. 19, 1263–1279.
Schratz, P., Muenchow, J., Iturritxa, E., Richter, J., Brenning, A., 2019. Hyperparameter tuning and performance assessment of statistical and machine-learning algorithms using spatial data. Ecol. Model. 406, 109–120.
Scotti, R., Brardinoni, F., Alberti, S., Frattini, P., Crosta, G.B., 2013. A regional inventory of rock glaciers and protalus ramparts in the central Italian Alps. Geomorphology 186, 136–149.
Shean, D., 2017. High Mountain Asia 8-Meter DEM Mosaics Derived from Optical Imagery, Version 1. Nasa National Snow and Ice Data Center Distributed Active Archive Center, Boulder, Colorado USA.
Villarroel, C.D., Tamburini Beliveau, G., Forte, A.P., Monserrat, O., Morvillo, M., 2018. DInSAR for a regional inventory of active rock glaciers in the dry Andes mountains of Argentina and Chile with sentinel-1 data. Remote Sens. 10, 1588.
Wahrhaftig, C., Cox, A., 1959. Rock glaciers in the Alaska range. GSA Bull. 70 (4), 383–436.
Wang, X.W., Liu, L., Zhao, L., Wu, T. H., Li, Z. Q. & Liu, G. X., 2017. Mapping and inventorying active rock glaciers in the Northern Tien Shan of China using satellite SAR interferometry. Cryosphere 11, 997–1014.
Xiang, Y., Gao, Y., Yao, T., 2014. Glacier change in the Poiqu River basin inferred from Landsat data from 1975 to 2010. Quat. Int. 349, 392–401.
Xu, H., 2006. Modification of normalised difference water index (NDWI) to enhance open water features in remotely sensed imagery. Int. J. Remote Sens. 27 (14), 3025–3033.
Yu, H., Ma, Y., Wang, L., Zhai, Y., Wang, X., 2017. A landslide intelligent detection method based on CNN and RSG_R. In: 2017 IEEE International Conference on Mechatronics and Automation (ICMA). 2017. pp. 40–44 6–9 Aug.
Zemp, M., Huss, M., Thibert, E., Eckert, N., Mcnabb, R., Huber, J., Barandun, M., Machguth, H., Nussbaumer, S.U., Gärtner-Roer, I., 2019. Global glacier mass changes and their contributions to sea-level rise from 1961 to 2016. Nature 568 (7752), 382–386.
Zhang, C., Sargent, I., Pan, X., Li, H.P., Gardiner, A., Hare, J., Atitinson, P.M., 2018. An object-based convolutional neural network (OCNN) for urban land use classification. Remote Sens. Environ. 216, 57–70.
Zhang, C., Yue, P., Tapete, D., Shangguan, B., Wang, M., Wu, Z., 2020. A multi-level context-guided classification method with object-based convolutional neural network for land cover classification using very high resolution remote sensing images. Int. J. Appl. Earth Obs. Geoinf. 88, 102086.
Zhang, L., Zhang, L., Du, B., 2016. Deep learning for remote sensing data: a technical tutorial on the state of the art. IEEE Geosci. Remote Sens. Mag. 4, 22–40.